PHYSICS

Measurement-based preparation of multimode mechanical states

Chao Meng[1], George A. Brawley[1,2], Soroush Khademi[1], Elizabeth M. Bridge[1], James S. Bennett[1], Warwick P. Bowen[1]*

Copyright © 2022 The Authors, some rights reserved; exclusive licensee American Association for the Advancement of Science. No claim to original U.S. Government Works. Distributed under a Creative Commons Attribution NonCommercial License 4.0 (CC BY-NC).

Nanomechanical resonators are a key tool for future quantum technologies, such as quantum force sensors and interfaces, and for studies of macroscopic quantum physics. The ability to prepare room temperature nonclassical states is a major outstanding challenge. It has been suggested that this could be achieved using a fast continuous measurement to break the usual symmetry between position and momentum. Here, we demonstrate this symmetry breaking and use it to prepare a thermally squeezed mechanical state. Our experiments take advantage of collective measurements on multiple mechanical modes, which we show can increase the measurement speed and improve state preparation. Theoretically, we show that this result extends to the quantum regime, relaxing the requirements to generate nonclassical states. We predict that multimode conditioning can enable room temperature quantum squeezing with existing technology. Our work paves the way toward room temperature quantum nanomechanical devices and toward their application in quantum technology and fundamental science.

INTRODUCTION

Quantum measurement is widely used to prepare nonclassical states and has important applications in quantum technologies from deterministic quantum computing (*1*, *2*) to quantum sensing (*3*, *4*) and fundamental tests of quantum mechanics (*5*, *6*). A common scenario is continuous linear measurement of the position of a linearly damped harmonic oscillator (*7*, *8*). This results in a Gaussian conditional state and, in the usual operating regime, localizes the position and momentum equally (*9*–*12*). Hence, it allows ground-state cooling (*10*–*14*) but precludes the generation of nonclassical states such as quantum squeezed states, where either the position or momentum is localized with better precision than the zero-point motion. It has recently been predicted that the symmetry between position and momentum can be broken if the rate of the measurement is sufficiently fast (*15*) and that this can allow quantum squeezing with greatly relaxed requirements compared to other approaches (*16*, *17*).

Here, we demonstrate this symmetry breaking, using continuous measurement to prepare and verify a thermomechanical squeezed state. We do this by exploiting collective measurements on multiple mechanical modes of a tailor-engineered optomechanical device. The presence of multiple mechanical modes has generally been considered an obstacle to measurement-based mechanical state preparation, with previous experiments limited to a single mode (*18*). We show experimentally that proper accounting for additional modes results in an increased measurement rate and therefore improved state preparation. We, further, show that the measurement introduces correlations between subensembles of mechanical modes, a precursor to the generation of entanglement between them.

To explore the limits of multimode state preparation, we derive theoretical conditions for both quantum squeezing and entanglement, predicting that collective measurements can greatly relax the requirements to prepare these nonclassical states. Our mechanical resonances exhibit structural damping (*19*, *20*), an important form of nonstandard decoherence for which measurement-based state preparation has not previously been achieved. We develop the theory for state preparation in the presence of such damping and find, perhaps unexpectedly, that it also relaxes the requirements to prepare nonclassical states. Together, our results predict that quantum squeezing is within the reach of existing technology, even at room temperature. This provides a path toward the widespread application of mechanical resonators in areas ranging from quantum sensing (*3*, *4*) to tests of fundamental physics (*5*, *21*, *22*).

RESULTS

Optomechanical device

A schematic of our multimode optomechanical experiment is shown in Fig. 1A. The optomechanical device is a 70-μm-diameter double-disk resonator, consisting of two vertically stacked silica microdisks, that naturally supports mechanical modes of various frequencies and provides high optomechanical coupling. Unlike previous double disks, the structure is engineered to maximally isolate the two lowest-frequency mechanical modes (the fundamental symmetric and antisymmetric flapping modes) from higher-frequency modes. This allows measurement-based state preparation to be explored on two relatively isolated modes before considering a larger ensemble. The key features of the design, arrived at via multiparameter finite-element optimization (see Materials and Methods), are an asymmetric opening through the interior of each disk and a centrally offset pedestal. Together, they result in a frequency separation that is 1.8 times larger than previous double-disk designs [e.g., (*23*)]. Note that this choice of a sparse mode structure is not optimal in the sense of permitting the best conditional variances, for which the optimum choice would be for the mechanical modes to be degenerate (see Materials and Methods). Rather, it facilitates unambiguous identification of the properties of each mechanical mode in the measured power spectrum. In our experiments, this is desirable to accurately determine the filter used to condition the mechanical state.

[1]Australian Research Council Centre of Excellence for Engineered Quantum Systems, School of Mathematics and Physics, The University of Queensland, St Lucia, Queensland 4072, Australia. [2]Terra15 Technologies Pty Ltd., Level 9/256 Adelaide Terrace, Perth, Western Australia 6000, Australia.
*Corresponding author. Email: w.bowen@uq.edu.au

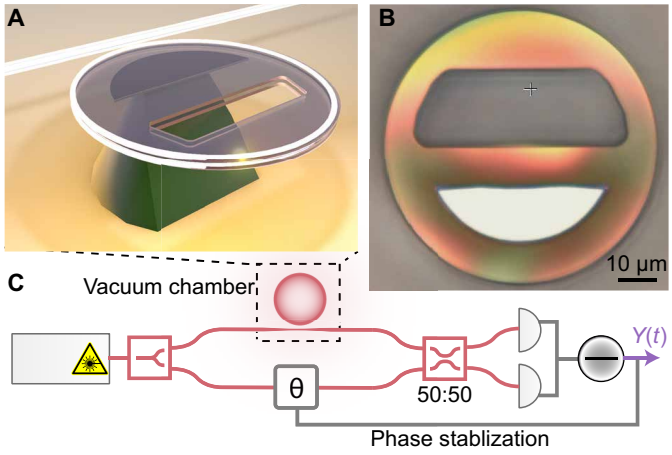

Fig. 1. Experimental apparatus. (**A**) Illustration of the structurally engineered double-disk optomechanical resonator and tapered fiber used for optical excitation. (**B**) Microscope image of the optomechanical resonator. The key dimensions of the resonator are the following: diameter, 70 μm; thickness, 400 nm; and separation between the disks, ~300 nm. (**C**) Schematic of homodyne measurement of optomechanical system. The laser is tuned onto resonance with the optomechanical resonator. The optomechanical device is housed in a vacuum chamber (pressure $<10^{-6}$ mbar), as indicated by the black dashed box. The photocurrent $Y(t)$ is digitized on an oscilloscope and stored for post-processing.

Our tailor-engineered double disk is fabricated using electron beam lithography following the process outlined in (*24*, *25*). An optical microscope image is shown in Fig. 1B. The device supports hybridized optical whispering gallery modes, resulting in optical resonance frequencies that are highly sensitive to the motion of the disk edges, especially in the vertical direction (*23*). We couple an optical double-disk resonance with a decay rate of $\kappa/2\pi = 2.8$ GHz to a fiber-based Mach-Zehnder interferometer as shown in Fig. 1C. Performing homodyne detection returns a photocurrent that is proportional to the phase quadrature of the output optical field. The power spectral density of this photocurrent (shown for the two lowest-frequency mechanical modes in Fig. 2, A and B) allows us to establish the resonance frequency Ω_j, decay rate Γ_j, and (boosted) optomechanical coupling rate $g_j = \sqrt{\mu_j \kappa}/2$ of each mechanical mode of the double disk (labeled by the subscript j), where $\mu_j = C_j\Gamma_j$ is the mode's optomechanical measurement rate (*9*), with C_j its optomechanical cooperativity. The average thermal occupancy of each mode $n_{\mathrm{th},\,j} \approx k_B T/\hbar\Omega_j$ is determined by assuming that the system is in thermal equilibrium at room temperature T, while finite element simulations provide the effective mass $m_{\mathrm{eff},\,j}$.

Structural damping

Analysis of the observed power spectral density allows us to identify that the mechanical modes of our double-disk device are structurally damped. The power spectrum of thermal noise driving a resonator is given by $S_{FF}^{\mathrm{th}}(\omega) = 2\,n_{\mathrm{th}}\,\Omega^2\,\phi(\omega)/\omega$, where ω is the angular frequency and $\phi(\omega)$ is the loss angle (*20*, *26*, *27*).

In contrast to viscous damping, where the loss angle is linearly dependent on frequency and results in a flat thermal noise spectrum, simple models of structural damping have a frequency-independent loss angle ($\phi = Q^{-1}$, where $Q = \Omega/\Gamma$ is the mechanical quality factor). As a consequence, the thermal noise spectrum of structural damping shows a characteristic inverse-frequency (or "1/*f*") dependence (*20*, *27*). We observe this 1/*f* dependence for the fundamental antisymmetric flapping mode over a frequency range from 10 to 200 kHz. As shown in Fig. 2A, the spectrum deviates from that expected for a viscously damped oscillator by more than an order of magnitude at low frequencies, while other noise sources are more than 30 dB below the measured thermal noise level over most of the measured frequency range (see the Supplementary Materials). Similarly, we find that a structural damping model accurately fits interferences observed between higher-frequency modes in the power spectral density, while an accurate fit is not possible using a viscously damped model (see the Supplementary Materials).

It is known that the simple 1/*f* noise model of structural damping is not physically realistic, violating the fluctuation-dissipation theorem (*26*) and causing the mechanical position spectrum to diverge at low frequencies. This results in both an infinite position variance and infinite energy, prohibiting formal estimation of the mechanical state. Rather than the frequency independence of usual structural damping models, for physically realistic damping mechanisms, the loss angle must be an odd function of ω to satisfy the fluctuation-dissipation theorem (*26*, *28*). Hence, it must pass through zero at $\omega = 0$, causing a low-frequency plateau in the thermomechanical noise. To our knowledge, no experimental or theoretical determination has previously been made of the frequency at which the transition to this plateau occurs nor is the exact low-frequency functional form of ϕ known.

Without prior knowledge of the functional form of the loss angle, to allow state estimation, we choose the simple modification $\phi = \omega Q^{-1}/\sqrt{\omega^2 + \omega_c^2}$. This is a smooth function of frequency that satisfies the fluctuation-dissipation theorem, is approximately constant above the roll-off frequency ω_c, as required from observations of structural damping, and scales linearly with frequency beneath ω_c as required to enforce a low-frequency plateau in the thermomechanical noise. Enforcing canonical thermal equilibrium $\int_{-\infty}^{+\infty} S_{qq}\,d\omega = n_{\mathrm{th}} + 1/2$ allows us to constrain ω_c for this postulated form of the loss angle. Fitting the power spectrum of the fundamental antisymmetric flapping mode, we find that the thermal occupation is within 2% of the room temperature thermal occupancy for roll-off frequencies between 1 and 10 kHz, so that $\omega_c/2\pi$ most likely lies in this range. The state preparation is found to be robust to the choice of roll-off frequency within this range (Supplementary Materials). For the results reported in Results, and Materials and Methods of the paper, we choose $\omega_c/2\pi = 10$ kHz for all modes.

Collective modes of motion

Our system is far in the unresolved sideband regime for all mechanical modes that we consider ($\kappa \gg \Omega_j\,\forall\,j$). In this regime, the homodyne-detected optical phase quadrature is (*9*)

$$Y = 2\sqrt{\eta\mu^{(N)}}\,q^{(N)} + \text{measurement noise} \qquad (1)$$

where η is the measurement efficiency and $\mu^{(N)} = \sum_j^N \mu_j$ is the collective optomechanical measurement rate. This provides a linear readout of the N-mode collective position operator $q^{(N)} = \sum_j^N \sqrt{\mu_j}\,q_j/\sqrt{\mu^{(N)}}$, where q_j is mode j's dimensionless position operator and is normalized such that the zero-point motion has a variance of 1/2. The superscript "(N)" is used throughout to represent the number of conditioned mechanical modes, although we suppress it when it is clear from context. All mechanical modes not included in $q^{(N)}$ contribute to the measurement noise, which also encompasses vacuum

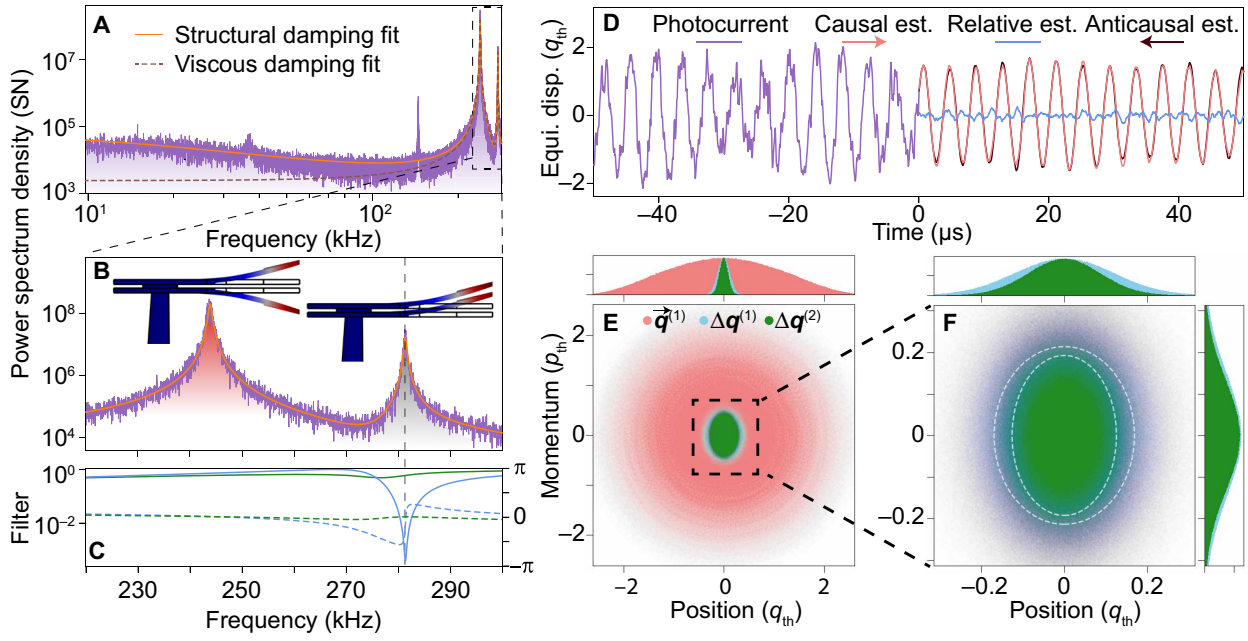

Fig. 2. Preparation of single- and two-mode mechanical states of a structurally damped resonator. (**A**) Power spectral density of thermal noise (purple) and fitted curves using structural damping (orange) and viscous damping (brown dashed line), normalized such that the shot noise (SN) level is 1/2. (**B**) Zoom-in of the thermal noise power spectral density (purple) of the first two mechanical modes. Red (gray) shading indicates the fundamental antisymmetric (symmetric) flapping mode. These modes are calibrated to have $(\eta\mu_1, \Omega_1, \Gamma_1)/2\pi = (0.74,244,0.69)$ kHz and $(\eta\mu_2, \Omega_2, \Gamma_2)/2\pi = (0.053,281,0.50)$ kHz, respectively. (**C**) Normalized absolute squared amplitude (solid line, left axis) and phase (dashed line, right axis) of filter functions. Blue, single-mode estimation; green, two-mode estimation. (**D**) Time traces of the photocurrent (purple), the causal (pink) and anticausal (maroon) position estimates of the first mechanical mode, and the corresponding relative estimate (blue), normalized by the standard deviation (SD) of the thermal fluctuations, $q_{th} = \left(\int_{-\infty}^{\infty} S_{qq}(\omega)\, d\omega/2\pi\right)^{1/2}$. (**E**) Phase space distributions of the unconditional state (pink) and relative single- and two-mode estimated states (blue and green, respectively), where $q = (q, p)$. The axes are normalized to the SD of the thermal position and momentum $\left(p_{th} = \left(\int_{-\infty}^{\infty} S_{pp}(\omega)\, d\omega/2\pi\right)^{1/2}\right)$ fluctuations. (**F**) Magnified phase space distributions of the one- and two-mode relative estimates. White dashed ellipses show their respective probability distribution contours (1/*e* of the maximum probability). (E and F) Histograms (4 million data points) of the position and momentum distributions, which obey Gaussian statistics.

fluctuations, classical laser phase noise, and electronic noise arising in the photodetector and amplifiers. A collective momentum $p^{(N)}$ can be defined by analogy to $q^{(N)}$ to satisfy the canonical commutation relation, $[q^{(N)}, p^{(N)}] = i$.

Conditional state preparation and verification

To perform conditional state preparation, we construct optimal causal Wiener filters for the position and momentum of the collective mechanical mode under study and apply them to the measurement data. A commonly used alternative is Kalman filtering (*13*, *18*). However, unlike Wiener filtering, this requires detailed knowledge of the temporal dynamics of the system. This is not available for structurally damped systems because they lack a widely accepted linear time domain model (*29*).

We construct the causal Wiener filter for the collective position $q^{(N)}$ by separating the measured power spectral density into a signal component from the mechanical mode(s) that participate in the collective mode and a noise component arising from all other mechanical modes, shot noise, classical phase noise, etc., as in Eq. 1. The filter can then be calculated as

$$\vec{H}_q(\omega) = \frac{1}{M_Y}\left[\frac{S_{qY}}{M_Y^*}\right]_+ \tag{2}$$

where the forward (right) arrow indicates that the estimate is causal, i.e., it estimates the current state from data recorded at earlier times. The cross-spectral density $S_{qY}(\omega)$ is calculated on the basis of the fitted optomechanical parameters of the estimated mode(s), and the causal spectral factor $M_Y(\omega)$ is numerically generated from a fit to the entire measured power spectrum. $[\cdots]_+$ denotes the causal part of the contained function. An analogous procedure is used to generate the causal Wiener filter for the collective momentum, $\vec{H}_p(\omega)$.

Applying the causal Wiener filters to the measured photocurrent yields causal estimates of the position and momentum. For example, the causal position estimate is $\vec{q}^{(N)}(t) = \vec{H}_q^{(N)}(t) \circledast Y(t)$, where $\vec{H}_q^{(N)}(t)$ is the collective position filter and $\circledast$ denotes a convolution. To quantify the uncertainty in the estimates, it is necessary to calculate the variances of their deviation from the true values. For example, the conditional position variance is given by $V_{\delta\vec{q}\delta\vec{q}} = \langle (q^{(N)} - \vec{q}^{(N)})^2 \rangle$. Unlike the estimates of the position and momentum themselves, the variances cannot be directly obtained because the "true" position $q^{(N)}$ and momentum $p^{(N)}$ are experimentally inaccessible. Instead, the prepared conditional state must be verified via comparison to a second set of independent estimates. We use anticausal filters ($\overleftarrow{H}_q$ and $\overleftarrow{H}_p$), which estimate the current position and momentum from measurement data at later (future) times, i.e., they perform retrodiction. These are labeled by a backward (left) arrow. The anticausal estimate of position, for example, is calculated as $\overleftarrow{q}^{(N)}(t) = \overleftarrow{H}_q^{(N)}(t) \circledast Y(t)$.

Following Rossi *et al.* (*18*), we define the relative position and momentum estimates, $\Delta q(t) = \vec{q}^{(N)} - \overleftarrow{q}^{(N)}$ and $\Delta p = \vec{p}^{(N)} - \overleftarrow{p}^{(N)}$. The conditional variances have generally been thought to be related

to the variances of these relative estimates by a simple factor of 2 (*18*). However, we find that this simple relationship does not hold for structural damping (see Materials and Methods). In general, the variances can be related by $V_{\Delta q \Delta q} = 2(1 - F_q) V_{\delta\vec{q}\delta\vec{q}}$ and $V_{\Delta p \Delta p} = 2(1 - F_p) V_{\delta\vec{p}\delta\vec{p}}$, where the conversion factors F_q and F_p characterize the deviation from a factor of 2. We use simulations to determine these conversion factors for each collective mode studied. We refer the reader to the Supplementary Materials for details on our prediction and retrodiction procedures.

Single-mode estimation

We begin by optimally estimating the position $q^{(1)}$ and momentum $p^{(1)}$ of only the (lowest frequency) fundamental antisymmetric flapping mode, with all other mechanical modes treated as noise. The magnitude response of the optimal causal Wiener filter for $q^{(1)}$ is shown by the blue trace in Fig. 2C. Wiener filters act to accept frequency components with high signal to noise and to reject those with low signal to noise. This is illustrated by the deep notch around the frequency of the fundamental symmetric flapping mode. To show the effect of the Wiener filter in the time domain, we compare the measured optical phase quadrature as a function of time before and after filtering. The left side of Fig. 2D shows the raw (normalized) phase quadrature Y. The thermally driven fundamental antisymmetric flapping mode is the dominant mechanical contribution, due to its strong optomechanical coupling, but its motion is partially obscured by measurement noise and the dynamics of the other mechanical modes. On the other hand, the pink trace on the right side of Fig. 2D shows the optimal causal estimate of the position $\vec{q}^{(1)}(t)$ as a function of time, calculated by applying the filter as described above $\left(\vec{q}^{(1)}(t) = \vec{H}_q^{(1)}(t) \circledast Y(t)\right)$. As can be seen, applying the filter removes much of the noise present in the unfiltered trace. The dark red trace shows the anticausally estimated position. This agrees closely with the causal estimate, as quantified by the relative estimate (blue trace).

Figure 2E plots the relative estimates in mechanical phase space, together with the direct position and momentum estimates. This allows the effect of single-mode conditioning on the mechanical state to be directly visualized. The phase space distribution of the direct estimates is consistent with a room temperature thermal state, as expected. The relative estimates, magnified in the phase space distribution of Fig. 2F, are confined much more closely near the origin. This is an example of "cooling by measurement" (*30*).

After determining the conversion factors $F_q^{(1)} = 0.26$ and $F_p^{(1)} = -0.11$, we find that the position and momentum conditional variances are $V_{\delta\vec{q}\delta\vec{q}}^{(1)} = (2.5 \pm 0.2) \times 10^5$ and $V_{\delta\vec{p}\delta\vec{p}}^{(1)} = (2.7 \pm 0.2) \times 10^5$, respectively. These results agree with simulations within their uncertainties, which are estimated using Monte Carlo propagation of the fitted optomechanical parameters (see the Supplementary Materials). They are also robust to the choice of roll-off frequency—a full order of magnitude change in ω_C (over the range from 1 to 10 kHz) changes the position and momentum variances by only ±10 and ±1%, respectively (see the Supplementary Materials). The conditional variances are reduced by factors of 9.7×10^{-3} and 10×10^{-3}, respectively, compared to the thermal variance of the mode, showing substantial conditional cooling. An upper bound on the conditional phonon occupancy of the mode can be calculated as $\bar{n}_{\mathrm{cond}} < \left(V_{\delta\vec{q}\delta\vec{q}}^{(1)} + V_{\delta\vec{p}\delta\vec{p}}^{(1)} - 1\right)/2 = 10 \times 10^{-3}\, n_{\mathrm{th}}$. Thus, the fundamental antisymmetric flapping mode is conditionally cooled by at least two orders of magnitude.

Note that, while the phase space distributions of Fig. 2 (E and F) appear to show notable thermomechanical squeezing, this is, in part, an artifact of the differences between the conversion factors for position and momentum. When conditioning only the first mode, this asymmetry falls below the uncertainty in the estimates once the relative variances are converted into conditional variances; the ratio of momentum to position variances is 1.7 ± 0.2 for the relative variances but only 1.1 ± 0.1 for the conditional variances. This highlights the importance of correctly accounting for the relationship between variances.

The low level of thermomechanical squeezing also highlights the detrimental effects of the higher-order mechanical modes on the estimation process. For an isolated viscously damped resonator, the squeezing criterion is $S = 16\,\mu n_{\mathrm{tot}} \Gamma/\Omega^2 > 1$, where $n_{\mathrm{tot}} = n_{\mathrm{th}} + C + 1/2$ is the total effective occupancy of the mode. This criterion was first obtained by Chen (*31*) and later, using the Wiener filter treatment and definition of measurement rate used here, by Meng *et al.* (*15*). By numerical simulation, we find that it can also be applied to the structural damping case. The criterion indicates that a high measurement rate, a large total effective occupancy, and a low resonance frequency are all advantageous to achieve thermal squeezing. The benefit of a low resonance frequency can be understood because this determines that the time delay before the (directly measured) position of the oscillator is converted to momentum. The longer the period of the oscillator, the more information the measurement extracts about position before it starts to yield momentum information (*15*).

For our experiments, the fundamental antisymmetric flapping mode has $S = 3.5 \times 10^3 \gg 1$. Consistent with this, our simulations show that, were the fundamental antisymmetric flapping mode well isolated from all other modes, the conditional state should be extremely strongly squeezed, having a ratio of momentum to position variances of 60. The problem of the presence of additional mechanical modes can be avoided, for example, by using a single-mode pendulum system; parallel experiments by Matsumoto and Yamamoto (*32*) have demonstrated single-mode thermomechanical squeezing, although without state verification. As we will show in what follows, multimode conditioning provides an alternative and more generally applicable solution.

Multimode estimation

Multimode conditioning achieves two closely related goals: It reclassifies the higher-order modes from noise to signal and, in the process, increases the effective measurement strength (*33*–*37*). We first examine the two-mode case, estimating the collective position and momenta of the well frequency-separated fundamental symmetric and antisymmetric flapping modes. Including these two modes increases the effective (inefficiency-reduced) optomechanical measurement rate from $\eta\mu^{(1)}/2\pi = 0.86$ kHz to $\eta\mu^{(2)}/2\pi = 0.91$ kHz. The causal Wiener filter for the collective position, calculated via Eq. 2, is shown in green in Fig. 2C. Applying this filter and its anticausal counterpart, we find that the collective conditional position variance of this two-mode collective mode is $V_{\delta\vec{q}\delta\vec{q}}^{(2)} = (1.6 \pm 0.1) \times 10^5$ with $F_q^{(2)} = 0.39$. Similarly, we find a collective momentum variance of $V_{\delta\vec{p}\delta\vec{p}}^{(2)} = (2.0 \pm 0.2) \times 10^5$ with $F_p^{(2)} = -0.18$. These variances are, respectively, 6.4×10^{-3} and 7.9×10^{-3} times smaller than the two-mode thermal variance and are improved by factors of 1.6 and 1.4, respectively, compared to single-mode estimation. Because the two-mode estimate reduces the variance in (collective) position

more than in momentum, it increases the thermomechanical squeezing. This results in a statistically significant level of squeezing, with a ratio of momentum to position variances of 1.2 ± 0.1. A similar improvement in squeezing of the relative estimates is seen in phase space (green dots) in Fig. 2 (E and F).

Our two-mode estimate, while superior to a single-mode estimate, is still roughly a factor of 400 inferior to predictions from simulations with no other mechanical modes present in the detected photocurrent. The state preparation can be improved further by including a larger number of mechanical modes in the collective mode. As an example, we select the first five modes, shown with red shading in the power spectral density in Fig. 3A. The combination of strong optomechanical coupling (*6*, *38*) and the intrinsic nonlinearity of the optomechanical measurement introduces several nonlinear peaks in this frequency region. The power contained in these (gray shaded) contributions is well below that of the linear peaks and more than 30 dB below the fundamental mechanical mode. The measurement signal is therefore dominated by the linear measurement signal, allowing the nonlinear peaks to be safely treated as noise. Treating them as noise, the optimal causal Wiener filter for the position of the five-mode collective mode is shown in Fig. 3B. It exhibits a broadband response, with slow modulations due to changes in the signal-to-noise ratio and several sharp notches that arise because of noise peaks in the power spectral density (shaded gray in Fig. 3A).

Applying the five-mode Wiener filter, the analogous filter for momentum, and the counterpart anticausal filters results in the experimental relative conditional state visualized in Fig. 3C. As can be seen, the five-mode collective state breaks the rotating wave approximation more strongly than the one- and two-mode states, being significantly more elliptical in phase space. This can be expected because it has a collective measurement rate of $\eta\mu^{(5)}/2\pi = 1.0$ kHz, higher than the measurement rates for either single- or two-mode cases. We calculate the conditional position variance to be $V^{(5)}_{\delta\vec{q}\delta\vec{q}} = (1.1 \pm 0.1) \times 10^5$, 5.0×10^{-3} times smaller than the five-mode thermal variance, with $F^{(5)}_q = 0.21$. The ratio of momentum to position conditional variances is found to be 2.3 ± 0.2, almost a factor of 2 larger than the two-mode case. Increasing the number of modes to nine further improves the measurement rate and thermal squeezing ratio to $\eta\mu^{(9)}/2\pi = 1.3$ kHz and 2.7 ± 0.2, respectively (see the Supplementary Materials).

The better conditioning that we achieve using collective mechanical modes implies that the measurement is inducing conditional correlations between the mechanical modes. We show these correlations experimentally, choosing to examine position-position and momentum-momentum correlations between two collective modes. The collective modes that we choose are the two-mode collective mode comprising the lowest- and second lowest-frequency modes (position, $q^{(2)}$; momentum, $p^{(2)}$) and the three-mode collective mode composed of the third, fourth, and fifth lowest-frequency modes, with collective position and momentum denoted here as $q^{(*3)}$ and $p^{(*3)}$, respectively. Figure 3D plots the relative position estimates of the two collective modes against each other, while Fig. 3E plots the relative momentum estimates.

A negative correlation of $\langle \Delta q^{(2)} \Delta q^{(*3)} \rangle / \sqrt{\langle \Delta q^{(2)\,2} \rangle \langle \Delta q^{(*3)\,2} \rangle} = -0.38$ is observed between the relative collective positions, while a positive correlation of +0.09 is observed between momenta, calculated in the same way. The fact that the observed correlations are of opposite sign suggests that stronger measurements could generate

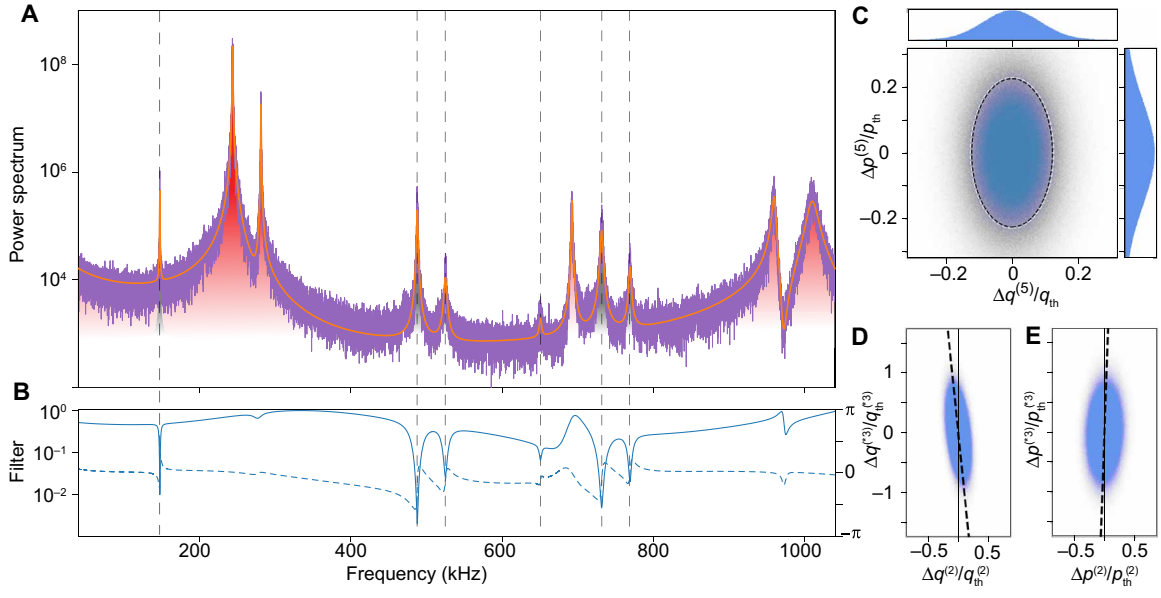

Fig. 3. Preparation of five-mode mechanical states. (**A**) Power spectral density of thermal noise (purple) and fitted curve using structurally damped model (orange). The red shaded areas are mechanical peaks and gray ones are noise peaks, including nonmechanical peaks and those arising from nonlinear optomechanical terms. The lowest frequency of these noise peaks is not of mechanical origin modeled with Lorentzian power spectra, and the other five originate from nonlinearities in the optomechanical interaction modeled with structural damping power spectra. They are all treated as noise. (**B**) Normalized absolute square amplitude (solid line, left axis) and phase (dashed line, right axis) of the filter function for conditioning the five mechanical modes. The filter function response notches out all the noise peaks (indicated by the vertical dashed lines). (**C**) Phase space distribution of the relative estimates of the five mechanical modes. Black and white dashed circles show the probability distribution contours (1/*e* of the maximum probability) from simulation and experiment, respectively, with very close agreement. (**D** and **E**) Position and momentum correlations between the relative estimates of collective modes made up of the lowest- and second lowest-frequency mechanical modes and the third, fourth, and fifth lowest-frequency modes, with normalized correlations of −0.38 and 0.09, respectively.

conditional entanglement. In Materials and Methods, we show that this is indeed possible for viscous damping, deriving the entanglement condition for N identical modes, $C > n_{th}^2 Q/2N\eta$.

DISCUSSION

Our work demonstrates the preparation of multimode mechanical states by continuous measurement, beyond previous work focused on single viscously damped resonators (*6*, *18*, *32*). The use of multimode conditioning allows operation outside the usual rotating wave approximation and thereby the generation of thermomechanical squeezed states. While our work operates very much in the classical regime, this breaking of the rotating wave approximation verifies a crucial theoretical prediction for the generation of quantum squeezed states of mechanical resonators at room temperature (*15*). We have also shown that the measurement generates conditional correlations between the position and momentum of different ensembles of mechanical modes. This is a key precursor for the generation of multimode mechanical entanglement, for which we derive an analytic condition.

It is interesting to ask how multimode conditioning and structural damping might affect the ability to generate quantum squeezing. It is known that measurements of the collective motion of multiple mechanical modes yield a larger effective measurement strength than single-mode measurements (*33*–*37*, *39*). However, to our knowledge, whether this can allow more effective quantum squeezing has not previously been addressed. Similarly, by reducing the high-frequency thermal noise of a mechanical resonator, structural damping has been shown to relax the requirements to observe radiation pressure backaction (*20*) and to achieve quantum squeezing of light (*40*). However, one might expect that the ability to prepare nonclassical mechanical states would be degraded by the increased low-frequency thermomechanical noise introduced by structural damping as well as by any correlations that structural damping creates with the mechanical environment.

To address these questions, in Materials and Methods, we theoretically model a collective optomechanical measurement of N mechanical modes. We find analytically that, for identical modes, the use of multiple modes relaxes the required cooperativity to achieve quantum squeezing by a factor of $1/N$ compared to a single mode, a result that holds for both structurally and viscously damped resonators. We also show that this result is robust to variations in the resonance frequencies of the modes. Our simulations show, somewhat remarkably, that in the thermal noise–dominated regime ($n_{th} \gg C$), the cooperativity needed for quantum squeezing is also lower for a structural damped resonator than for a viscously damped one, in this case reduced by a factor of $(Q/n_{th})^{1/12}$. Together, we find that quantum squeezing is achievable for a structurally damped multimode resonator so long as $C > n_{tot}^{(N)1/4} Q^{3/4}/N\eta$, where $n_{tot}^{(N)} = n_{th} + NC + 1/2$ is the total thermal occupancy of the collective mechanical mode.

The theoretical calculations of the previous paragraph show that structural damping and multimode conditioning can substantially reduce the requirements for quantum squeezing and therefore may allow it to be achieved at room temperature. To examine the experimental feasibility of this, we consider a multimode structurally damped zipper cavity device of the form reported by Leijssen *et al.* (*38*). The zipper device had a mechanical frequency $\Omega/2\pi = 3$ MHz, a single-photon optomechanical coupling strength of $g_0/2\pi = 24$ MHz, and mechanical and optical decay rates of $\Gamma/2\pi = 100$ Hz and $\kappa/2\pi = 20$ GHz, respectively. For a single mechanical resonance and assuming a detection efficiency of $\eta = 0.5$, these parameters should allow room temperature conditioning of quantum squeezed states using only 160 intracavity photons. Were an array of N identical resonators used, the required intracavity photon number would drop by $1/N$. It should be noted that the very large optomechanical coupling provided by this device leads to large optomechanical nonlinearity at room temperature. Nevertheless, Wiener filtering can still be used for state preparation, provided that the measurement record is linearized. This can be achieved by using a second, much weaker laser to perform feedback cooling, reducing the amplitude of motion into the linear regime, analogous to the scheme used in (*41*). Hence, our results open a pathway to room temperature quantum squeezing and to room temperature quantum optomechanical technologies, such as quantum force sensors and interfaces, and to explore the crossover between quantum and classical physics.

An alternative approach to achieving room temperature quantum squeezing would be to use a suspended mass system such as those found in gravitational wave detectors (*42*). This provides the dual advantages of exceptionally low frequency, in the range of 1 Hz (*43*), and of the simplicity associated with having only a single well isolated mechanical mode. With the high optical powers available to gravitational wave detectors, it is conceivable that room temperature quantum squeezing may be possible (*15*, *44*) and that this may have benefits for the detection of gravitational waves or tests of fundamental physics. A major advantage of our approach is that the mechanical resonator is fabricated on a silicon chip and can be integrated with other on-chip technologies. This provides the prospect of applications in chip-scale quantum sensing and computing (*7*, *9*, *45*, *46*).

A substantial technical advance in our paper is the development of a method to perform state preparation on structurally damped resonators and, in the process, to determine the roll-off frequency of structural damping. Structural damping is encountered in many macroscopic engineered structures (*26*, *29*, *47*) and has been observed in a range of optomechanical systems (*20*, *27*, *48*–*50*). It is thought to be non-Markovian; however, there is no widely accepted model for its origins (*19*). To our knowledge, the transition to a flat thermomechanical noise spectrum at low frequencies that is required to satisfy thermodynamics has never been observed in experiments. Our use of the equipartition theorem to constrain the value of the transition frequency, even when it is beneath experimentally resolvable frequencies, therefore provides a means to access new information about structural damping. Together, these possibilities provide a new route toward understanding the underlying mechanisms that give rise to this widespread and relatively poorly understood form of damping (*19*).

MATERIALS AND METHODS

Optomechanical system and measurement

Our tailor-engineered double disks have been optimized to maximize the frequency separation of adjacent mechanical modes; this is achieved by incorporating off-center slots that result in asymmetric pinning, a key characteristic that differs from previous designs (*23*–*25*). Qualitatively speaking, this forces the mechanical modes to behave more like those of a singly clamped cantilever, which are widely separated in frequency. Specifically, typical symmetrically

clamped double-disk resonators exhibit a pair of low-frequency modes, with the next mode occurring at a frequency around 1.6 times the frequency of the fundamental (lowest-frequency) mode (*51*). By comparison, in our asymmetrically clamped double disks, this third mode is shifted up to 2.9 times the fundamental frequency. This increased separation is in close alignment to the case for a singly clamped cantilever oscillator, for which the third mode is at approximately three times the fundamental frequency.

The asymmetric pinning in our tailor-engineered double-disk design acts to lengthen the mechanical arms of the oscillator, which lowers the frequencies of the fundamental mechanical modes Ω_1 and Ω_2. This assists in the preparation of squeezed states, as discussed in (*15*). The slots in our double disk also act to reduce the effective mass ($m_{\mathrm{eff},1}$ = 536 pg for the fundamental antisymmetric flapping mode). As a result, our design increases the zero-point motion of fundamental mode by a factor of 2.1 compared to a spiderweb double disk (*23*) and 5.7 compared to a solid double disk (*51*, *52*). Counteracting these improvements, the asymmetric pinning suppresses motion on one half of the disk, reducing the optomechanical coupling strength by a factor of 3.6 to 4.3 GHz/nm, a reduction which is consistent with our experimental observations (*51*). Overall, by permitting the thermal noise of the two lowest-frequency modes to dominate the power spectral density over a larger bandwidth than a comparable symmetrical double disk, our design allows better estimation of the motion of the collective mode that consists of the lowest- and second lowest-frequency modes.

A continuous-wave diode laser running at the wavelength of 1555 nm is resonant with the whispering-gallery mode of the double-disk device. For a fixed optical power injected into the optomechanical system, it is desirable to work near the critical coupling point, where the intrinsic cavity energy damping rate κ_0 is equal to the input-output coupling rate κ_{ex}, because this maximizes the effective measurement rate $\mu \propto \kappa_{ex}^2/(\kappa_0 + \kappa_{ex})^4$. In practice, we couple the light in and out by positioning a tapered optical fiber close to the perimeter of the double disk. Positioning limitations means that we operate in the slightly overcoupled regime, with $\kappa_0/2\pi$ = 1.0 GHz and $\kappa_{ex}/2\pi$ = 1.8 GHz. Injecting 3.7 μW of optical power results in 4300 intracavity photons. The total detection efficiency is η = 30% (including the escape efficiency of 64%, fiber transmission of 67%, taper transmission of 89%, and detector quantum efficiency of 80%).

Double-disk design optimization

The geometry of the double-disk structure is optimized to maximize the ratio of the frequencies of the high-order modes to the fundamental flapping modes. As the symmetric and antisymmetric fundamental modes are close to each other in frequency, and because our fabrication technique leads to roughly identical slot shape and size on both top and bottom disks, we simplified the model by simulating one disk with one slot. For a fixed diameter of disk, the mechanical frequencies are affected by the location and geometry of the slot and of the sandwich layer between the disks (which acts as a clamping point for the mechanical motion). We choose the slot geometry to be a half-circle with a flattened top, as shown in Fig. 4A. The flattened top reduces the width of the slot and increases the effective mass of the fundamental mode without significantly changing its spring constant. This decreases its frequency. On the other hand, it can stiffen the higher-frequency modes and has a smaller effect on their effective masses. Together, this results in an increased frequency separation compared to alternative double-disk designs.

The slot geometry is defined by the mask used in electron beam lithography. The radius of the circular part is chosen to ensure that the rim of the disk is wide enough to contain the whispering gallery modes of the device and therefore that the slot does not introduce large optical losses. In fabrication, the etchant reaches the sandwich layer both from outside the disk and by diffusing through the slot. This results in the semicircular sandwich layer geometry shown in Fig. 4A. By tuning the duration of the etch, we are able to tune the width of the sandwich layer.

Given that the slot and sandwich layer widths can both be tuned in fabrication, we perform finite-element simulations to investigate what the optimum choice of these two parameters is to maximally separate the frequency of the fundamental mode from the higher-frequency modes. Specifically, we determine the ratio of the frequency of the lowest-frequency mode to that of the second lowest mode, as a function of slot and sandwich layer widths. We note that including two disks, rather than the one modeled here, the lowest-frequency mode separates into the symmetric and antisymmetic fundamental modes that we observe in the experiment. The results of the simulation are shown in Fig. 4B, where the sandwich and slot widths are normalized to the diameter of the disk. As can be seen, the maximum mode separation of around a factor of 3 occurs when the slot width and sandwich width are both around 20% of the disk diameter.

Model of multimode state preparation with viscous damping

To understand theoretically how collective measurements on multiple modes differ from the single-mode measurements considered by Meng *et al.* (*15*), we restrict ourselves to the simple case where the mechanical modes are identical (equal C, Ω, Γ, etc.). It is then possible to directly use the results of Meng *et al.* (*15*) to predict the effectiveness of localization of a viscously damped collective mode; one need only make the simple replacement $C \to NC$. We find that the rotating wave approximation breaks down when $C > Q^2/N\eta n_{\mathrm{tot}}^{(N)}$. The breakdown of the rotating wave approximation and therefore generation of thermal squeezing occur at cooperativities a factor of N lower than those found by Meng *et al.* (*15*). Moreover, we find that—deep within the regime where the rotating wave approximation

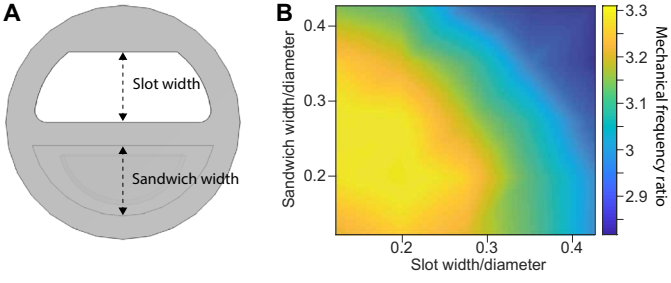

Fig. 4. Optimization of the structure of the double disk. (**A**) Diagram of the engineered structure. The widths of the slot and sandwich layers are labeled with black dashed lines. The half circle inside the sandwich layer represents the top of the pedestal that supports the double disk. This is narrower than the sandwich layer due to the faster etch rate of the pedestal. (**B**) Color map of the ratio of the frequencies of the second to first mechanical eigenmode as a function of the slot and sandwich layer widths, normalized to the diameter of the disk.

breaks down—the conditional variance of the collective position becomes

$$V_{\delta q \delta q}^{(N)} \approx \left[\frac{Q^2 n_{\mathrm{tot}}^{(N)}}{64(\eta N C)^3}\right]^{1/4} \quad (3)$$

Compared to the single-mode case, this variance is reduced by a factor of $N^{3/4}$ in the thermal noise–dominated regime and $N^{1/2}$ in the backaction-dominated regime.

The purity of the conditional state of $\mathcal{P} = \sqrt{\eta N C / n_{\mathrm{tot}}}$ is increased but saturates to the same value in the backaction-dominated regime. We see therefore that collective measurements on multiple mechanical oscillators can both greatly relax the requirement to prepare a nonclassical state and improve the quality of the nonclassical state that is prepared.

Within the regime of validity of the rotating wave approximation, collective measurements on multiple mechanical modes can also improve cooling by measurement. Specifically, the condition for when the ground state of a viscously damped resonator is approached is relaxed by a factor of N to $C > n_{\mathrm{th}}/N\eta$.

Model of state preparation with structural damping

For structurally damped resonators, we begin by modeling a single-mode mechanical resonator and extend to the multimode case in the same way as in the viscous damping case treated above. To make qualitative conclusions, we consider continuous position measurement and numerically calculate the conditional position variance as a function of C and n_{th} (assuming unity detection efficiency). The results are shown in Fig. 5. Note that the results are almost independent of the choice of ω_C; for the single-mode case here, there is less than 0.1% change in conditional variance as ω_C is swept from 1 to 10 kHz. Here, we fix the bath at room temperature so that an increase in n_{th} corresponds to a decrease in the mechanical frequency. We observe that quantum squeezing can be achieved when $C > n_{\mathrm{tot}}^{1/4} Q^{3/4}/\eta$ (black dashed line in Fig. 5), i.e., with lower C compared to a single-mode viscously damped oscillator in the thermal noise–dominated regime (*15*) (white dashed line in Fig. 5). For N identical structurally damped modes, the quantum squeezing criterion is relaxed to $C > n_{\mathrm{tot}}^{(N)1/4} Q^{3/4}/N\eta$ by replacing $C \to NC$, as in the viscous damping case.

To explore a more general case where the mechanical modes are nondegenerate, we numerically considered a multimode oscillator constructed from a set of mechanical resonators whose resonance frequencies are equally spaced with a separation $\Delta\Omega$ around a central frequency $\bar{\Omega}$. The linewidths and central frequency were held fixed. As seen in Fig. 6, a larger separation of mode frequencies does indeed degrade the conditional position variance but only gently. This implies that the required measurement strength for quantum squeezing will only slightly increase for the nondegenerate multimode case compared to the degenerate case. A more comprehensive treatment is beyond the scope of this paper.

Relationship between relative and conditional variances for a structurally damped resonator

In our experiments, the conditional state is prepared and verified using prediction and retrodiction. In the case of a single viscously damped resonator and in the limit of a high measurement rate, the conditional variance is equal to half the variance of the difference between the estimates produced via prediction and retrodiction

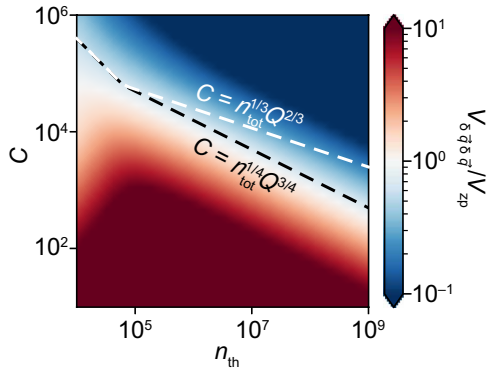

Fig. 5. Simulation of the conditional position variance of a single-mode structurally damped resonator under continuous position measurement. The state becomes conditionally quantum squeezed above the black dashed line. The threshold for quantum squeezing of a single-mode viscously damped resonator is shown for comparison by the white dashed line. We see that structural damping results in relaxed experimental requirements to achieve quantum squeezing in the regime where $C \ll n_{\mathrm{th}}$.

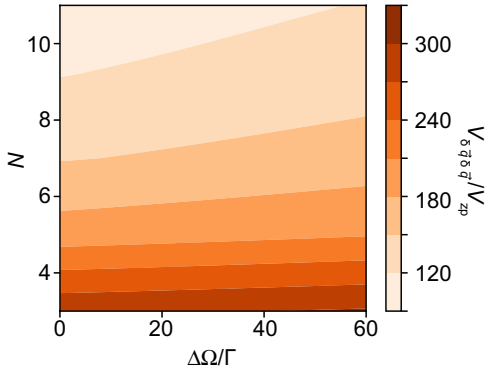

Fig. 6. Characterization of the conditional position variance in terms of mode number *N* and mode separation ΔΩ. The optomechanical parameters used here are similar to the antisymmetrical flapping mode of our tailor-engineered double disk. The multiple modes have a fixed mean frequency, $\bar{\Omega}/2\pi = 240$ kHz, and linewidths. They are separated by equal increments of $\Delta\Omega$. Each mode has $\eta C = 1$ and $\Gamma/2\pi = 0.7$ kHz.

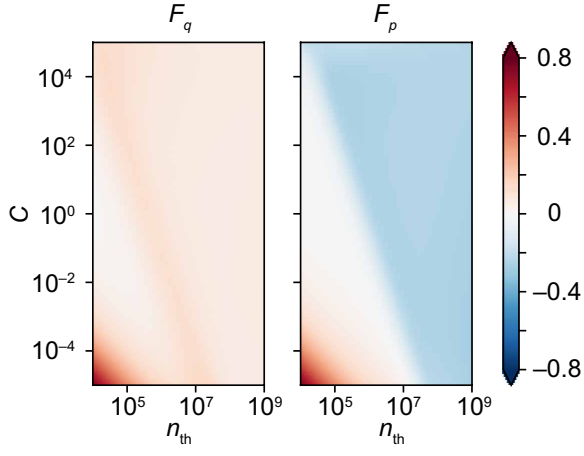

Fig. 7. Characterization of the conversion factors F_q and F_p for a single-mode structurally damped oscillator as a function of n_{th} (fixing the bath at room temperature) and *C*.

(i.e., the variance of the relative estimate) (*18*). However, we observe that this is not the case for a structurally damped oscillator even in the high measurement regime. As a result, characterization of the conversion factors F_q and F_p is essential to obtain the conditional state. We characterize them via simulations. As an example, Fig. 7 shows both conversion factors as a function of the thermal occupancy and cooperativity. As can be seen, F_p becomes negative at sufficiently high cooperativities, with the regime over which this occurs roughly coinciding with the regime where the rotating wave approximation is invalid. F_q, on the other hand, is always positive but is nonzero at high cooperativities.

Analysis of measurement-induced entanglement

In our discussion of measurement-induced entanglement in the main text, we consider a specific form of entanglement in which an even number N of identical mechanical modes (equal C, Ω, Γ, etc.) is measured. The common position $(q_1 + q_2 + q_3 + q_4 \ldots q_{N-1} + q_N)$ is strongly conditioned (as discussed above). Conversely, the differential momentum $(p_1 - p_2 + p_3 - p_4 \ldots + p_{N-1} - p_N)$ is entirely decoupled from the dynamics of the common position (this follows from Ω being equal for all modes), so the measurement provides no information about the differential momentum. Furthermore, every mechanical mode is driven by the same radiation pressure noise, resulting in no net backaction on the differential momentum; contributions from every odd mode $(p_1, p_3, \ldots)$ are exactly cancelled by the even modes $(p_2, p_4, \ldots)$. As a result, the conditional momentum of the differential mode is equal to its unconditional (thermal) momentum, $V^{(N-)}_{\delta\vec{p}\delta\vec{p}} = n_{\mathrm{th}} + 1/2$. The criterion $V^{(N)}_{\delta\vec{q}\delta\vec{q}} V^{(N-)}_{\delta\vec{p}\delta\vec{p}} < 1/4$ is a sufficient criterion for entanglement (*9*). Using the thermal momentum and Eq. 3, this leads to the condition for the two collective modes to become conditionally entangled, as stated in the main text.

SUPPLEMENTARY MATERIALS

Supplementary material for this article is available at https://science.org/doi/10.1126/sciadv.abm7585

REFERENCES AND NOTES

1. E. Knill, R. Laflamme, G. J. Milburn, A scheme for efficient quantum computation with linear optics. *Nature* **409**, 46–52 (2001).
2. D. Ristè, M. Dukalski, C. A. Watson, G. de Lange, M. J. Tiggelman, Y. M. Blanter, K. W. Lehnert, R. N. Schouten, L. DiCarlo, Deterministic entanglement of superconducting qubits by parity measurement and feedback. *Nature* **502**, 350–354 (2013).
3. K. C. Cox, G. P. Greve, J. M. Weiner, J. K. Thompson, Deterministic squeezed states with collective measurements and feedback. *Phys. Rev. Lett.* **116**, 093602 (2016).
4. C. Sayrin, I. Dotsenko, X. Zhou, B. Peaudecerf, T. Rybarczyk, S. Gleyzes, P. Rouchon, M. Mirrahimi, H. Amini, M. Brune, J.-M. Raimond, S. Haroche, Real-time quantum feedback prepares and stabilizes photon number states. *Nature* **477**, 73–77 (2011).
5. Z. K. Minev, S. O. Mundhada, S. Shankar, P. Reinhold, R. Gutiérrez-Jáuregui, R. J. Schoelkopf, M. Mirrahimi, H. J. Carmichael, M. H. Devoret, To catch and reverse a quantum jump mid-flight. *Nature* **570**, 200–204 (2019).
6. G. A. Brawley, M. R. Vanner, P. E. Larsen, S. Schmid, A. Boisen, W. P. Bowen, Nonlinear optomechanical measurement of mechanical motion. *Nat. Commun.* **7**, 10988 (2016).
7. M. Aspelmeyer, T. J. Kippenberg, F. Marquardt, Cavity optomechanics. *Rev. Mod. Phys.* **86**, 1391–1452 (2014).
8. V. B. Braginsky, Y. I. Vorontsov, K. S. Thorne, Quantum nondemolition measurements. *Science* **209**, 547–557 (1980).
9. W. P. Bowen, G. J. Milburn, *Quantum Optomechanics* (CRC Press, 2015).
10. A. C. Doherty, A. Szorkovszky, G. I. Harris, W. P. Bowen, The quantum trajectory approach to quantum feedback control of an oscillator revisited. *Philos. Trans. A Math. Phys. Eng. Sci.* **370**, 5338–5353 (2012).
11. D. J. Wilson, V. Sudhir, N. Piro, R. Schilling, A. Ghadimi, T. J. Kippenberg, Measurement-based control of a mechanical oscillator at its thermal decoherence rate. *Nature* **524**, 325–329 (2015).
12. M. Rossi, D. Mason, J. Chen, Y. Tsaturyan, A. Schliesser, Measurement-based quantum control of mechanical motion. *Nature* **563**, 53–58 (2018).
13. L. Magrini, P. Rosenzweig, C. Bach, A. Deutschmann-Olek, S. G. Hofer, S. Hong, N. Kiesel, A. Kugi, M. Aspelmeyer, Real-time optimal quantum control of mechanical motion at room temperature. *Nature* **595**, 373–377 (2021).
14. F. Tebbenjohanns, M. L. Mattana, M. Rossi, M. Frimmer, L. Novotny, Quantum control of a nanoparticle optically levitated in cryogenic free space. *Nature* **595**, 378–382 (2021).
15. C. Meng, G. A. Brawley, J. S. Bennett, M. R. Vanner, W. P. Bowen, Mechanical squeezing via fast continuous measurement. *Phys. Rev. Lett.* **125**, 043604 (2020).
16. M. Brunelli, D. Malz, A. Nunnenkamp, Conditional dynamics of optomechanical two-tone backaction-evading measurements. *Phys. Rev. Lett.* **123**, 093602 (2019).
17. A. Szorkovszky, A. C. Doherty, G. I. Harris, W. P. Bowen, Mechanical Squeezing via Parametric Amplification and Weak Measurement. *Phys. Rev. Lett.* **107**, 213603 (2011).
18. M. Rossi, D. Mason, J. Chen, A. Schliesser, Observing and verifying the quantum trajectory of a mechanical resonator. *Phys. Rev. Lett.* **123**, 163601 (2019).
19. S. Gröblacher, A. Trubarov, N. Prigge, G. D. Cole, M. Aspelmeyer, J. Eisert, Observation of non-Markovian micromechanical Brownian motion. *Nat. Commun.* **6**, 7606 (2015).
20. J. Cripe, N. Aggarwal, R. Lanza, A. Libson, R. Singh, P. Heu, D. Follman, G. D. Cole, N. Mavalvala, T. Corbitt, Measurement of quantum back action in the audio band at room temperature. *Nature* **568**, 364–367 (2019).
21. M. Arndt, K. Hornberger, Testing the limits of quantum mechanical superpositions. *Nat. Phys.* **10**, 271–277 (2014).
22. S. Forstner, M. Zych, S. Basiri-Esfahani, K. E. Khosla, W. P. Bowen, Nanomechanical test of quantum linearity. *Optica* **7**, 1427–1434 (2020).
23. J. Rosenberg, Q. Lin, O. Painter, Static and dynamic wavelength routing via the gradient optical force. *Nat. Photonics* **3**, 478–483 (2009).
24. C. Bekker, C. G. Baker, R. Kalra, H.-H. Cheng, B.-B. Li, V. Prakash, W. P. Bowen, Free spectral range electrical tuning of a high quality on-chip microcavity. *Opt. Express* **26**, 33649–33670 (2018).
25. C. J. Bekker, C. G. Baker, W. P. Bowen, Optically tunable photoluminescence and up-conversion lasing on a chip. *Phys. Rev. Appl.* **15**, 034022 (2021).
26. P. R. Saulson, Thermal noise in mechanical experiments. *Phys. Rev. D* **42**, 2437–2445 (1990).
27. S. A. Fedorov, V. Sudhir, R. Schilling, H. Schütz, D. J. Wilson, T. J. Kippenberg, Evidence for structural damping in a high-stress silicon nitride nanobeam and its implications for quantum optomechanics. *Phys. Lett. A* **382**, 2251–2255 (2018).
28. L. D. Landau, E. M. Lifshitz, *Statistical Physics, Third Edition, Part 1: Volume 5* (Butterworth-Heinemann, 1980).
29. C. W. De Silva, *Vibration Damping, Control, and Design* (Mechanical Engineering Series, Taylor & Francis, 2007).
30. M. R. Vanner, J. Hofer, G. D. Cole, M. Aspelmeyer, Cooling-by-measurement and mechanical state tomography via pulsed optomechanics. *Nat. Commun.* **4**, 2295 (2013).
31. Y. Chen, Macroscopic quantum mechanics: Theory and experimental concepts of optomechanics. *J. Phys. B* **46**, 104001 (2013).
32. N. Matsumoto, N. Yamamoto, Conditional mechanical squeezing of a macroscopic pendulum near quantum regimes. arXiv:2008.10848 [quant-ph] (25 August 2020).
33. A. Xuereb, C. Genes, A. Dantan, Collectively enhanced optomechanical coupling in periodic arrays of scatterers. *Phys. Rev. A* **88**, 053803 (2013).
34. T. Kipf, G. S. Agarwal, Superradiance and collective gain in multimode optomechanics. *Phys. Rev. A* **90**, 053808 (2014).
35. B. Nair, A. Xuereb, A. Dantan, Cavity optomechanics with arrays of thick dielectric membranes. *Phys. Rev. A* **94**, 053812 (2016).
36. P. Piergentili, L. Catalini, M. Bawaj, S. Zippilli, N. Malossi, R. Natali, D. Vitali, G. D. Giuseppe, Two-membrane cavity optomechanics. *New J. Phys.* **20**, 083024 (2018).
37. A. Xuereb, C. Genes, A. Dantan, Strong coupling and long-range collective interactions in optomechanical arrays. *Phys. Rev. Lett.* **109**, 223601 (2012).
38. R. Leijssen, G. R. La Gala, L. Freisem, J. T. Muhonen, E. Verhagen, Nonlinear cavity optomechanics with nanomechanical thermal fluctuations. *Nat. Commun.* **8**, 16024 (2017).
39. W. H. P. Nielsen, Y. Tsaturyan, C. B. Møller, E. S. Polzik, A. Schliesser, Multimode optomechanical system in the quantum regime. *Proc. Natl. Acad. Sci. U.S.A.* **114**, 62–66 (2017).
40. N. Aggarwal, T. J. Cullen, J. Cripe, G. D. Cole, R. Lanza, A. Libson, D. Follman, P. Heu, T. Corbitt, N. Mavalvala, Room-temperature optomechanical squeezing. *Nat. Phys.* **16**, 784–788 (2020).
41. G. I. Harris, U. L. Andersen, J. Knittel, W. P. Bowen, Feedback-enhanced sensitivity in optomechanics: Surpassing the parametric instability barrier. *Phys. Rev. A* **85**, 061802 (2012).
42. B. P. Abbott, R. Abbott, T. D. Abbott, M. R. Abernathy, F. Acernese, K. Ackley, C. Adams, T. Adams, P. Addesso, R. X. Adhikari, V. B. Adya, C. Affeldt, M. Agathos, K. Agatsuma, N. Aggarwal, O. D. Aguiar, L. Aiello, A. Ain, P. Ajith, B. Allen, A. Allocca, P. A. Altin, S. B. Anderson, W. G. Anderson, K. Arai, M. A. Arain, M. C. Araya, C. C. Arceneaux,

J. S. Areeda, N. Arnaud, K. G. Arun, S. Ascenzi, G. Ashton, M. Ast, S. M. Aston, P. Astone, P. Aufmuth, C. Aulbert, S. Babak, P. Bacon, M. K. M. Bader, P. T. Baker, F. Baldaccini, G. Ballardin, S. W. Ballmer, J. C. Barayoga, S. E. Barclay, B. C. Barish, D. Barker, F. Barone, B. Barr, L. Barsotti, M. Barsuglia, D. Barta, J. Bartlett, M. A. Barton, I. Bartos, R. Bassiri, A. Basti, J. C. Batch, C. Baune, V. Bavigadda, M. Bazzan, B. Behnke, M. Bejger, C. Belczynski, A. S. Bell, C. J. Bell, B. K. Berger, J. Bergman, G. Bergmann, C. P. L. Berry, D. Bersanetti, A. Bertolini, J. Betzwieser, S. Bhagwat, R. Bhandare, I. A. Bilenko, G. Billingsley, J. Birch, R. Birney, O. Birnholtz, S. Biscans, A. Bisht, M. Bitossi, C. Biwer, M. A. Bizouard, J. K. Blackburn, C. D. Blair, D. G. Blair, R. M. Blair, S. Bloemen, O. Bock, T. P. Bodiya, M. Boer, G. Bogaert, C. Bogan, A. Bohe, P. Bojtos, C. Bond, F. Bondu, R. Bonnand, B. A. Boom, R. Bork, V. Boschi, S. Bose, Y. Bouffanais, A. Bozzi, C. Bradaschia, P. R. Brady, V. B. Braginsky, M. Branchesi, J. E. Brau, T. Briant, A. Brillet, M. Brinkmann, V. Brisson, P. Brockill, A. F. Brooks, D. A. Brown, D. D. Brown, N. M. Brown, C. C. Buchanan, A. Buikema, T. Bulik, H. J. Bulten, A. Buonanno, D. Buskulic, C. Buy, R. L. Byer, M. Cabero, L. Cadonati, G. Cagnoli, C. Cahillane, J. Calderón Bustillo, T. Callister, E. Calloni, J. B. Camp, K. C. Cannon, J. Cao, C. D. Capano, E. Capocasa, F. Carbognani, S. Caride, J. Casanueva Diaz, C. Casentini, S. Caudill, M. Cavaglià, F. Cavalier, R. Cavalieri, G. Cella, C. B. Cepeda, L. Cerboni Baiardi, G. Cerretani, E. Cesarini, R. Chakraborty, T. Chalermsongsak, S. J. Chamberlin, M. Chan, S. Chao, P. Charlton, E. Chassande-Mottin, H. Y. Chen, Y. Chen, C. Cheng, A. Chincarini, A. Chiummo, H. S. Cho, M. Cho, J. H. Chow, N. Christensen, Q. Chu, S. Chua, S. Chung, G. Ciani, F. Clara, J. A. Clark, F. Cleva, E. Coccia, P.-F. Cohadon, A. Colla, C. G. Collette, L. Cominsky, M. Constancio Jr., A. Conte, L. Conti, D. Cook, T. R. Corbitt, N. Cornish, A. Corsi, S. Cortese, C. A. Costa, M. W. Coughlin, S. B. Coughlin, J.-P. Coulon, S. T. Countryman, P. Couvares, E. E. Cowan, D. M. Coward, M. J. Cowart, D. C. Coyne, R. Coyne, K. Craig, J. D. E. Creighton, T. D. Creighton, J. Cripe, S. G. Crowder, A. M. Cruise, A. Cumming, L. Cunningham, E. Cuoco, T. Dal Canton, S. L. Danilishin, S. D'Antonio, K. Danzmann, N. S. Darman, C. F. Da Silva Costa, V. Dattilo, I. Dave, H. P. Daveloza, M. Davier, G. S. Davies, E. J. Daw, R. Day, S. De, D. De Bra, G. Debreczeni, J. Degallaix, M. De Laurentis, S. Deléglise, W. Del Pozzo, T. Denker, T. Dent, H. Dereli, V. Dergachev, R. T. De Rosa, R. De Rosa, R. De Salvo, S. Dhurandhar, M. C. Díaz, L. Di Fiore, M. Di Giovanni, A. Di Lieto, S. Di Pace, I. Di Palma, A. Di Virgilio, G. Dojcinoski, V. Dolique, F. Donovan, K. L. Dooley, S. Doravari, R. Douglas, T. P. Downes, M. Drago, R. W. P. Drever, J. C. Driggers, Z. Du, M. Ducrot, S. E. Dwyer, T. B. Edo, M. C. Edwards, A. Effler, H.-B. Eggenstein, P. Ehrens, J. Eichholz, S. S. Eikenberry, W. Engels, R. C. Essick, T. Etzel, M. Evans, T. M. Evans, R. Everett, M. Factourovich, V. Fafone, H. Fair, S. Fairhurst, X. Fan, Q. Fang, S. Farinon, B. Farr, W. M. Farr, M. Favata, M. Fays, H. Fehrmann, M. M. Fejer, D. Feldbaum, I. Ferrante, E. C. Ferreira, F. Ferrini, F. Fidecaro, L. S. Finn, I. Fiori, D. Fiorucci, R. P. Fisher, R. Flaminio, M. Fletcher, H. Fong, J.-D. Fournier, S. Franco, S. Frasca, F. Frasconi, M. Frede, Z. Frei, A. Freise, R. Frey, V. Frey, T. T. Fricke, P. Fritschel, V. V. Frolov, P. Fulda, M. Fyffe, H. A. G. Gabbard, J. R. Gair, L. Gammaitoni, S. G. Gaonkar, F. Garufi, A. Gatto, G. Gaur, N. Gehrels, G. Gemme, B. Gendre, E. Genin, A. Gennai, J. George, L. Gergely, V. Germain, A. Ghosh, A. Ghosh, S. Ghosh, J. A. Giaime, K. D. Giardina, A. Giazotto, K. Gill, A. Glaefke, J. R. Gleason, E. Goetz, R. Goetz, L. Gondan, G. González, J. M. Gonzalez Castro, A. Gopakumar, N. A. Gordon, M. L. Gorodetsky, S. E. Gossan, M. Gosselin, R. Gouaty, C. Graef, P. B. Graff, M. Granata, A. Grant, S. Gras, C. Gray, G. Greco, A. C. Green, R. J. S. Greenhalgh, P. Groot, H. Grote, S. Grunewald, G. M. Guidi, X. Guo, A. Gupta, M. K. Gupta, K. E. Gushwa, E. K. Gustafson, R. Gustafson, J. J. Hacker, B. R. Hall, E. D. Hall, G. Hammond, M. Haney, M. M. Hanke, J. Hanks, C. Hanna, M. D. Hannam, J. Hanson, T. Hardwick, J. Harms, G. M. Harry, I. W. Harry, M. J. Hart, M. T. Hartman, C.-J. Haster, K. Haughian, J. Healy, J. Heefner, A. Heidmann, M. C. Heintze, G. Heinzel, H. Heitmann, P. Hello, G. Hemming, M. Hendry, I. S. Heng, J. Hennig, A. W. Heptonstall, M. Heurs, S. Hild, D. Hoak, K. A. Hodge, D. Hofman, S. E. Hollitt, K. Holt, D. E. Holz, P. Hopkins, D. J. Hosken, J. Hough, E. A. Houston, E. J. Howell, Y. M. Hu, S. Huang, E. A. Huerta, D. Huet, B. Hughey, S. Husa, S. H. Huttner, T. Huynh-Dinh, A. Idrisy, N. Indik, D. R. Ingram, R. Inta, H. N. Isa, J.-M. Isac, M. Isi, G. Islas, T. Isogai, B. R. Iyer, K. Izumi, M. B. Jacobson, T. Jacqmin, H. Jang, K. Jani, P. Jaranowski, S. Jawahar, F. Jiménez-Forteza, W. W. Johnson, N. K. Johnson-McDaniel, D. I. Jones, R. Jones, R. J. G. Jonker, L. Ju, K. Haris, C. V. Kalaghatgi, V. Kalogera, S. Kandhasamy, G. Kang, J. B. Kanner, S. Karki, M. Kasprzack, E. Katsavounidis, W. Katzman, S. Kaufer, T. Kaur, K. Kawabe, F. Kawazoe, F. Kéfélian, M. S. Kehl, D. Keitel, D. B. Kelley, W. Kells, R. Kennedy, D. G. Keppel, J. S. Key, A. Khalaidovski, F. Y. Khalili, I. Khan, S. Khan, Z. Khan, E. A. Khazanov, N. Kijbunchoo, C. Kim, J. Kim, K. Kim, N.-G. Kim, N. Kim, Y.-M. Kim, E. J. King, P. J. King, D. L. Kinzel, J. S. Kissel, L. Kleybolte, S. Klimenko, S. M. Koehlenbeck, K. Kokeyama, S. Koley, V. Kondrashov, A. Kontos, S. Koranda, M. Korobko, W. Z. Korth, I. Kowalska, D. B. Kozak, V. Kringel, B. Krishnan, A. Królak, C. Krueger, G. Kuehn, P. Kumar, R. Kumar, L. Kuo, A. Kutynia, P. Kwee, B. D. Lackey, M. Landry, J. Lange, B. Lantz, P. D. Lasky, A. Lazzarini, C. Lazzaro, P. Leaci, S. Leavey, E. O. Lebigot, C. H. Lee, H. K. Lee, H. M. Lee, K. Lee, A. Lenon, M. Leonardi, J. R. Leong, N. Leroy, N. Letendre, Y. Levin, B. M. Levine, T. G. F. Li, A. Libson, T. B. Littenberg, N. A. Lockerbie, J. Logue, A. L. Lombardi, L. T. London, J. E. Lord, M. Lorenzini, V. Loriette, M. Lormand, G. Losurdo, J. D. Lough, C. O. Lousto, G. Lovelace, H. Lück, A. P. Lundgren, J. Luo, R. Lynch, Y. Ma, T. Mac Donald, B. Machenschalk, M. Mac Innis, D. M. Macleod, F. Magaña-Sandoval, R. M. Magee, M. Mageswaran, E. Majorana, I. Maksimovic, V. Malvezzi, N. Man, I. Mandel, V. Mandic, V. Mangano, G. L. Mansell, M. Manske, M. Mantovani, F. Marchesoni, F. Marion, S. Márka, Z. Márka, A. S. Markosyan, E. Maros, F. Martelli, L. Martellini, I. W. Martin, R. M. Martin, D. V. Martynov, J. N. Marx, K. Mason, A. Masserot, T. J. Massinger, M. Masso-Reid, F. Matichard, L. Matone, N. Mavalvala, N. Mazumder, G. Mazzolo, R. McCarthy, D. E. McClelland, S. McCormick, S. C. McGuire, G. McIntyre, J. McIver, D. J. McManus, S. T. McWilliams, D. Meacher, G. D. Meadors, J. Meidam, A. Melatos, G. Mendell, D. Mendoza-Gandara, R. A. Mercer, E. Merilh, M. Merzougui, S. Meshkov, C. Messenger, C. Messick, P. M. Meyers, F. Mezzani, H. Miao, C. Michel, H. Middleton, E. E. Mikhailov, L. Milano, J. Miller, M. Millhouse, Y. Minenkov, J. Ming, S. Mirshekari, C. Mishra, S. Mitra, V. P. Mitrofanov, G. Mitselmakher, R. Mittleman, A. Moggi, M. Mohan, S. R. P. Mohapatra, M. Montani, B. C. Moore, C. J. Moore, D. Moraru, G. Moreno, S. R. Morriss, K. Mossavi, B. Mours, C. M. Mow-Lowry, C. L. Mueller, G. Mueller, A. W. Muir, A. Mukherjee, D. Mukherjee, S. Mukherjee, N. Mukund, A. Mullavey, J. Munch, D. J. Murphy, P. G. Murray, A. Mytidis, I. Nardecchia, L. Naticchioni, R. K. Nayak, V. Necula, K. Nedkova, G. Nelemans, M. Neri, A. Neunzert, G. Newton, T. T. Nguyen, A. B. Nielsen, S. Nissanke, A. Nitz, F. Nocera, D. Nolting, M. E. N. Normandin, L. K. Nuttall, J. Oberling, E. Ochsner, J. O'Dell, E. Oelker, G. H. Ogin, J. J. Oh, S. H. Oh, F. Ohme, M. Oliver, P. Oppermann, R. J. Oram, B. O'Reilly, R. O'Shaughnessy, C. D. Ott, D. J. Ottaway, R. S. Ottens, H. Overmier, B. J. Owen, A. Pai, S. A. Pai, J. R. Palamos, O. Palashov, C. Palomba, A. Pal-Singh, H. Pan, Y. Pan, C. Pankow, F. Pannarale, B. C. Pant, F. Paoletti, A. Paoli, M. A. Papa, H. R. Paris, W. Parker, D. Pascucci, A. Pasqualetti, R. Passaquieti, D. Passuello, B. Patricelli, Z. Patrick, B. L. Pearlstone, M. Pedraza, R. Pedurand, L. Pekowsky, A. Pele, S. Penn, A. Perreca, H. P. Pfeiffer, M. Phelps, O. Piccinni, M. Pichot, M. Pickenpack, F. Piergiovanni, V. Pierro, G. Pillant, L. Pinard, I. M. Pinto, M. Pitkin, J. H. Poeld, R. Poggiani, P. Popolizio, A. Post, J. Powell, J. Prasad, V. Predoi, S. S. Premachandra, T. Prestegard, L. R. Price, M. Prijatelj, M. Principe, S. Privitera, R. Prix, G. A. Prodi, L. Prokhorov, O. Puncken, M. Punturo, P. Puppo, M. Pürrer, H. Qi, J. Qin, V. Quetschke, E. A. Quintero, R. Quitzow-James, F. J. Raab, D. S. Rabeling, H. Radkins, P. Raffai, S. Raja, M. Rakhmanov, C. R. Ramet, P. Rapagnani, V. Raymond, M. Razzano, V. Re, J. Read, C. M. Reed, T. Regimbau, L. Rei, S. Reid, D. H. Reitze, H. Rew, S. D. Reyes, F. Ricci, K. Riles, N. A. Robertson, R. Robie, F. Robinet, A. Rocchi, L. Rolland, J. G. Rollins, V. J. Roma, J. D. Romano, R. Romano, G. Romanov, J. H. Romie, D. Rosińska, S. Rowan, A. Rüdiger, P. Ruggi, K. Ryan, S. Sachdev, T. Sadecki, L. Sadeghian, L. Salconi, M. Saleem, F. Salemi, A. Samajdar, L. Sammut, L. M. Sampson, E. J. Sanchez, V. Sandberg, B. Sandeen, G. H. Sanders, J. R. Sanders, B. Sassolas, B. S. Sathyaprakash, P. R. Saulson, O. Sauter, R. L. Savage, A. Sawadsky, P. Schale, R. Schilling, J. Schmidt, P. Schmidt, R. Schnabel, R. M. S. Schofield, A. Schönbeck, E. Schreiber, D. Schuette, B. F. Schutz, J. Scott, S. M. Scott, D. Sellers, A. S. Sengupta, D. Sentenac, V. Sequino, A. Sergeev, G. Serna, Y. Setyawati, A. Sevigny, D. A. Shaddock, T. Shaffer, S. Shah, M. S. Shahriar, M. Shaltev, Z. Shao, B. Shapiro, P. Shawhan, A. Sheperd, D. H. Shoemaker, D. M. Shoemaker, K. Siellez, X. Siemens, D. Sigg, A. D. Silva, D. Simakov, A. Singer, L. P. Singer, A. Singh, R. Singh, A. Singhal, A. M. Sintes, B. J. J. Slagmolen, J. R. Smith, M. R. Smith, N. D. Smith, R. J. E. Smith, E. J. Son, B. Sorazu, F. Sorrentino, T. Souradeep, A. K. Srivastava, A. Staley, M. Steinke, J. Steinlechner, S. Steinlechner, D. Steinmeyer, B. C. Stephens, S. P. Stevenson, R. Stone, K. A. Strain, N. Straniero, G. Stratta, N. A. Strauss, S. Strigin, R. Sturani, A. L. Stuver, T. Z. Summerscales, L. Sun, P. J. Sutton, B. L. Swinkels, M. J. Szczepańczyk, M. Tacca, D. Talukder, D. B. Tanner, M. Tápai, S. P. Tarabrin, A. Taracchini, R. Taylor, T. Theeg, M. P. Thirugnanasambandam, E. G. Thomas, M. Thomas, P. Thomas, K. A. Thorne, K. S. Thorne, E. Thrane, S. Tiwari, V. Tiwari, K. V. Tokmakov, C. Tomlinson, M. Tonelli, C. V. Torres, C. I. Torrie, D. Töyrä, F. Travasso, G. Traylor, D. Trifirò, M. C. Tringali, L. Trozzo, M. Tse, M. Turconi, D. Tuyenbayev, D. Ugolini, C. S. Unnikrishnan, A. L. Urban, S. A. Usman, H. Vahlbruch, G. Vajente, G. Valdes, M. Vallisneri, N. van Bakel, M. van Beuzekom, J. F. J. van den Brand, C. Van Den Broeck, D. C. Vander-Hyde, L. van der Schaaf, J. V. van Heijningen, A. A. van Veggel, M. Vardaro, S. Vass, M. Vasúth, R. Vaulin, A. Vecchio, G. Vedovato, J. Veitch, P. J. Veitch, K. Venkateswara, D. Verkindt, F. Vetrano, A. Viceré, S. Vinciguerra, D. J. Vine, J.-Y. Vinet, S. Vitale, T. Vo, H. Vocca, C. Vorvick, D. Voss, W. D. Vousden, S. P. Vyatchanin, A. R. Wade, L. E. Wade, M. Wade, S. J. Waldman, M. Walker, L. Wallace, S. Walsh, G. Wang, H. Wang, M. Wang, X. Wang, Y. Wang, H. Ward, R. L. Ward, J. Warner, M. Was, B. Weaver, L.-W. Wei, M. Weinert, A. J. Weinstein, R. Weiss, T. Welborn, L. Wen, P. Weßels, T. Westphal, K. Wette, J. T. Whelan, S. E. Whitcomb, D. J. White, B. F. Whiting, K. Wiesner, C. Wilkinson, P. A. Willems, L. Williams, R. D. Williams, A. R. Williamson, J. L. Willis, B. Willke, M. H. Wimmer, L. Winkelmann, W. Winkler, C. C. Wipf, A. G. Wiseman, H. Wittel, G. Woan, J. Worden, J. L. Wright, G. Wu, J. Yablon, I. Yakushin, W. Yam, H. Yamamoto, C. C. Yancey, M. J. Yap, H. Yu, M. Yvert, A. Zadrożny, L. Zangrando, M. Zanolin, J.-P. Zendri, M. Zevin, F. Zhang, L. Zhang, M. Zhang, Y. Zhang, C. Zhao, M. Zhou, Z. Zhou, X. J. Zhu, M. E. Zucker, S. E. Zuraw, J. Zweizig; LIGO Scientific Collaboration and Virgo Collaboration, Observation of gravitational waves from a binary black hole merger. *Phys. Rev. Lett.* **116**, 061102 (2016).

43. C. Whittle, E. D. Hall, S. Dwyer, N. Mavalvala, V. Sudhir, R. Abbott, A. Ananyeva, C. Austin, L. Barsotti, J. Betzwieser, C. D. Blair, A. F. Brooks, D. D. Brown, A. Buikema, C. Cahillane, J. C. Driggers, A. Effler, A. Fernandez-Galiana, P. Fritschel, V. V. Frolov, T. Hardwick,

M. Kasprzack, K. Kawabe, N. Kijbunchoo, J. S. Kissel, G. L. Mansell, F. Matichard, L. McCuller, T. McRae, A. Mullavey, A. Pele, R. M. S. Schofield, D. Sigg, M. Tse, G. Vajente, D. C. Vander-Hyde, H. Yu, H. Yu, C. Adams, R. X. Adhikari, S. Appert, K. Arai, J. S. Areeda, Y. Asali, S. M. Aston, A. M. Baer, M. Ball, S. W. Ballmer, S. Banagiri, D. Barker, J. Bartlett, B. K. Berger, D. Bhattacharjee, G. Billingsley, S. Biscans, R. M. Blair, N. Bode, P. Booker, R. Bork, A. Bramley, K. C. Cannon, X. Chen, A. A. Ciobanu, F. Clara, C. M. Compton, S. J. Cooper, K. R. Corley, S. T. Countryman, P. B. Covas, D. C. Coyne, L. E. H. Datrier, D. Davis, C. di Fronzo, K. L. Dooley, P. Dupej, T. Etzel, M. Evans, T. M. Evans, J. Feicht, P. Fulda, M. Fyffe, J. A. Giaime, K. D. Giardina, P. Godwin, E. Goetz, S. Gras, C. Gray, R. Gray, A. C. Green, E. K. Gustafson, R. Gustafson, J. Hanks, J. Hanson, R. K. Hasskew, M. C. Heintze, A. F. Helmling-Cornell, N. A. Holland, J. D. Jones, S. Kandhasamy, S. Karki, P. J. King, R. Kumar, M. Landry, B. B. Lane, B. Lantz, M. Laxen, Y. K. Lecoeuche, J. Leviton, J. Liu, M. Lormand, A. P. Lundgren, R. Macas, M. MacInnis, D. M. Macleod, S. Márka, Z. Márka, D. V. Martynov, K. Mason, T. J. Massinger, R. McCarthy, D. E. McClelland, S. McCormick, J. McIver, G. Mendell, K. Merfeld, E. L. Merilh, F. Meylahn, T. Mistry, R. Mittleman, G. Moreno, C. M. Mow-Lowry, S. Mozzon, T. J. N. Nelson, P. Nguyen, L. K. Nuttall, J. Oberling, R. J. Oram, C. Osthelder, D. J. Ottaway, H. Overmier, J. R. Palamos, W. Parker, E. Payne, R. Penhorwood, C. J. Perez, M. Pirello, H. Radkins, K. E. Ramirez, J. W. Richardson, K. Riles, N. A. Robertson, J. G. Rollins, C. L. Romel, J. H. Romie, M. P. Ross, K. Ryan, T. Sadecki, E. J. Sanchez, L. E. Sanchez, T. R. Saravanan, R. L. Savage, D. Schaetz, R. Schnabel, E. Schwartz, D. Sellers, T. Shaffer, B. J. J. Slagmolen, J. R. Smith, S. Soni, B. Sorazu, A. P. Spencer, K. A. Strain, L. Sun, M. J. Szczepańczyk, M. Thomas, P. Thomas, K. A. Thorne, K. Toland, C. I. Torrie, G. Traylor, A. L. Urban, G. Valdes, P. J. Veitch, K. Venkateswara, G. Venugopalan, A. D. Viets, T. Vo, C. Vorvick, M. Wade, R. L. Ward, J. Warner, B. Weaver, R. Weiss, B. Willke, C. C. Wipf, L. Xiao, H. Yamamoto, L. Zhang, M. E. Zucker, J. Zweizig, Approaching the motional ground state of a 10-kg object. *Science* **372**, 1333–1336 (2021).

44. H. Müller-Ebhardt, On quantum effects in the dynamics of macroscopic test masses, thesis, Leibniz University Hannover (2009).
45. M. Pechal, P. Arrangoiz-Arriola, A. H. Safavi-Naeini, Superconducting circuit quantum computing with nanomechanical resonators as storage. *Quantum Sci. Technol.* **4**, 015006 (2019).
46. F. Pistolesi, A. Cleland, A. Bachtold, Proposal for a nanomechanical qubit. *Phys. Rev. X* **11**, 031027 (2021).
47. A. L. Kimball, D. E. Lovell, Internal friction in solids. *Phys. Rev.* **30**, 948–959 (1927).
48. A. R. Neben, T. P. Bodiya, C. Wipf, E. Oelker, T. Corbitt, N. Mavalvala, Structural thermal noise in gram-scale mirror oscillators. *New J. Phys.* **14**, 115008 (2012).
49. A. H. Safavi-Naeini, S. Gröblacher, J. T. Hill, J. Chan, M. Aspelmeyer, O. Painter, Squeezed light from a silicon micromechanical resonator. *Nature* **500**, 185–189 (2013).
50. K. Komori, Y. Enomoto, C. P. Ooi, Y. Miyazaki, N. Matsumoto, V. Sudhir, Y. Michimura, M. Ando, Attonewton-meter torque sensing with a macroscopic optomechanical torsion pendulum. *Phys. Rev. A* **101**, 011802 (2020).
51. J. Rosenberg, Applications of micro/nanoscale optical resonators: Plasmonic photodetectors and double-disk cavity optomechanics, thesis, California Institute of Technology, Pasadena, CA (2010).
52. Q. Lin, J. Rosenberg, X. Jiang, K. J. Vahala, O. Painter, Mechanical oscillation and cooling actuated by the optical gradient force. *Phys. Rev. Lett.* **103**, 103601 (2009).
53. N. Wiener, *Extrapolation, Interpolation, and Smoothing of Stationary Time Series* (The MIT Press, 1964).
54. R. G. Brown, P. Y. C. Hwang, *Introduction to Random Signals and Applied Kalman Filtering, 3rd Edition* (Wiley, 1996).
55. M. Tsang, J. H. Shapiro, S. Lloyd, Quantum theory of optical temporal phase and instantaneous frequency. II. Continuous-time limit and state-variable approach to phase-locked loop design. *Phys. Rev. A* **79**, 053843 (2009).
56. B. Fornberg, C. Piret, *Complex Variables and Analytic Functions: An Illustrated Introduction* (SIAM - Society for Industrial and Applied Mathematics, 2020).

Acknowledgments: We would like to thank E. H. H. Cheng, G. I. Harris, C. J. Bekker, C. G. Baker, and H. M. Wiseman for useful discussion. This work was performed, in part, at the Queensland node of the Australian National Fabrication Facility, a company established under the National Collaborative Research Infrastructure Strategy to provide nano- and microfabrication facilities for Australia's researchers. We acknowledge the facilities and the scientific and technical assistance of the Australian Microscopy and Microanalysis Research Facility at the Centre for Microscopy and Microanalysis, The University of Queensland. **Funding:** This research was supported by the Australian Research Council Centre of Excellence for Engineered Quantum Systems (EQUS, CE170100009). E.M.B. thanks EQUS for support and funding from an EQUS Deborah Jin Fellowship. **Author contributions:** The core concept was conceived by W.P.B., with refinements by C.M. and G.A.B. Tailor-engineered double-disk design and fabrication were performed by G.A.B. with input from C.M. and W.P.B. The optomechanical measurement apparatus was designed by G.A.B. and W.P.B., with C.M. and E.M.B. performing assembly and testing. C.M. collected the measurement data, with important contributions from G.A.B. and S.K. Data analysis methods were refined by C.M., G.A.B., J.S.B., S.K., and W.P.B. Analytical models were found by C.M., G.A.B., S.K., J.S.B., and W.P.B. The manuscript was primarily written by C.M., J.S.B., and W.P.B., with contributions from all authors. Figures were chiefly prepared by C.M. Primary supervision for this project was performed by W.P.B., with assistance from J.S.B. and E.M.B. **Competing interests:** The authors declare that they have no competing interests. **Data and materials availability:** All data needed to evaluate the conclusions in the paper are present in the paper and/or the Supplementary Materials.

Submitted 28 October 2021
Accepted 13 April 2022
Published 27 May 2022
10.1126/sciadv.abm7585